Journal of Energy Chemistry 26 (2017) 501–509

Contents lists available at ScienceDirect

Journal of Energy Chemistry

journal homepage: www.elsevier.com/locate/jechem

http://www.journals.elsevier.com/journal-of-energy-chemistry/

Different oxidation routes for lattice oxygen recovery of double-perovskite type oxides $LaSrFeCoO_6$ as oxygen carriers for chemical looping steam methane reforming

Kun Zhao[a,b,c], Yang Shen[b,c], Zhen Huang[a], Fang He[a,*], Guoqiang Wei[a,c], Anqing Zheng[a,c], Haibin Li[a,c], Zengli Zhao[a,c]

[a] Key Laboratory of Renewable Energy, Guangzhou Institute of Energy Conversion, Chinese Academy of Sciences, Guangzhou 510640, Guangdong, China
[b] Guangdong Key Laboratory of New and Renewable Energy Research and Development, Guangzhou Institute of Energy Conversion, Chinese Academy of Sciences, Guangzhou 510640, Guangdong, China
[c] University of Chinese Academy of Sciences, Beijing 100049, China

ARTICLE INFO

Article history:
Received 13 July 2016
Revised 30 September 2016
Accepted 1 November 2016
Available online 29 November 2016

Keywords:
Double-perovskite
Chemical looping
Lattice oxygen
Oxidizing agent
Redox

ABSTRACT

Double-perovskite type oxide $LaSrFeCoO_6$(LSFCO) was used as oxygen carrier for chemical looping steam methane reforming (CL-SMR) due to its unique structure and reactivity. Two different oxidation routes, steam-oxidation and steam-air-stepwise-oxidation, were applied to investigate the recovery behaviors of the lattice oxygen in the oxygen carrier. The characterizations of the oxide were determined by X-ray diffraction (XRD), X-ray photoelectron spectroscopy (XPS), hydrogen temperature-programmed reduction (H_2-TPR) and scanning electron microscopy (SEM). The fresh sample LSFCO exhibits a monocrystalline perovskite structure with cubic symmetry and high crystallinity, except for a little impurity phase due to the antisite defect of Fe/Co disorder. The deconvolution distribution of XPS patterns indicated that Co, and Fe are predominantly in an oxidized state (Fe^{3+} and Fe^{2+}) and (Co^{2+} and Co^{3+}), while O 1*s* exists at three species of lattice oxygen, chemisorbed oxygen and physical adsorbed oxygen. The double perovskite structure and chemical composition recover to the original state after the steam and air oxidation, while the Co ion cannot incorporate into the double perovskite structure and thus form the CoO just via individual steam oxidation. In comparison to the two different oxidation routes, the sample obtained by steam-oxidation exhibits even higher CH_4 conversion, CO and H_2 selectivity and stronger hydrogen generation capacity.

1. Introduction

As a subclass of perovskite-type oxides ABO_3, the double perovskite-type oxide $AA'BB'O_6$ have attracted more and more attentions as magnetic materials [1], superconducting materials [2], and catalytic materials [3–5], due to its unique structure and multiple properties. In the double perovskite-type $A'A''B'B''O_6$ structure, $B'-O_6$ and $B''-O_6$ octahedras are arranged alternately by the way of corner-sharing with A cations occupy the voids between the octahedral [6]. The sequence of $B'-O-B''$ chain is formed by B′ and B″ cations in an ideal double perovskite-type structure. While an order-reduced or disordered state is associated with a random distribution of $B'-O-B'$, $B'-O-B''$ or $B''-O-B''$ chains [7]. It is generally believed that the catalytic activity of double perovskite-type oxide is mainly decided by the B-site cations, while the A-site cations play a role in the controlling of valence state of B-site metals and stabilizing the structure, simultaneously causing the lattice defects [8]. Therefore the most interesting phenomenon in double perovskite-type oxide is the interaction and synergistic effects between the B′ and B″ cations. The catalytic activities of double perovskite-type oxides can be effectively improved through the synergy and coordination of the metals in the special structure and the different configurations and exchange interactions between A′/A″ and B′/B″ metals provide an extensive modeling space for researchers.

At present, chemical looping steam methane reforming (CL-SMR, as shown in Fig. 1) technology is mainly concentrated on the

Abbreviations: LSFCO, $LaSrFeCoO_6$; CL-SMR, chemical looping steam methane reforming; XRD, X-ray diffraction; XPS, X-ray photoelectron spectroscopy; H_2-TPR, hydrogen temperature-programmed reduction; SEM, scanning electron microscopy; LSFCO-S, reacted sample after CH_4–H_2O cycle; LSFCO-A, reacted sample after CH_4–H_2O-air cycle.

* Corresponding author. Fax: +86 2087057737.
E-mail address: hefang@ms.giec.ac.cn (F. He).

http://dx.doi.org/10.1016/j.jechem.2016.11.016

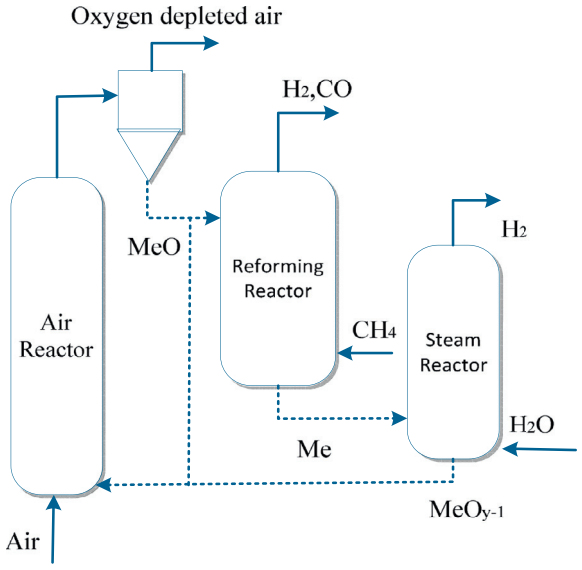

Fig. 1. CL-SMR for syngas and hydrogen production.

finding of excellent oxygen carriers with high methane conversion, high syngas selectivity, high sintering resistance and good activity for water splitting to produce hydrogen. In the CL-SMR process, methane is partially oxidized to syngas by the lattice oxygen of the oxygen carrier in the reformer reactor ($M_xO_y+CH_4 \rightarrow M_xO_{y-\delta1-\delta2}+(2H_2+CO)$), and the reduced oxygen carrier is oxidized by steam to recover oxygen and simultaneously to produce hydrogen in the steam reactor ($M_xO_{y-\delta1-\delta2}+H_2O \rightarrow M_xO_{y-\delta1}+H_2$). Usually, an air oxidation stage is needed if the oxygen carrier cannot completely recovery oxygen by steam oxidation ($M_xO_{y-\delta1}+O_2 \rightarrow M_xO_y$) [9–11]. Through this process, not only syngas was obtained, the environmental friendly energy carrier hydrogen also can be produced via two steps, without requiring additional gas treatments such as reforming or shifting and separation processes. In previous researches, various metals [12,13], complex metals [14,15], perovskite oxides [16–18] or double perovskite-type oxides [5] had been used as catalysts for methane conversion. Results showed that perovskite-type oxides exhibited excellent performance with high catalytic activity and stability. Various substitutions or doping of perovskite-type oxides are exploited to satisfy the requests for various needs. As mentioned above, double perovskite-type oxide is different from the single perovskite-type oxide with special B′-O–B″ or B″–O–B″ chains. As far as we know, there is no report dealing with the catalytic performance of double perovskite-type oxide for chemical looping steam methane reforming, especially from the points of both chemical reforming of methane and water splitting. Also the cyclic reactivity of double perovskite-type oxide for oxygen delivery has no research.

Generally, there are two kinds of oxygen species in the double perovskite-type oxide. One is the adsorbed oxygen that related to the defect oxides, or surface molecular oxygen with low coordination, which is beneficial to the complete oxidation of CH_4 to produce CO_2 and H_2O. Another is the lattice oxygen that is conducive to the partial oxidation of CH_4 for the generation of syngas. As an oxidizing agent, steam with lower activity just can guarantee the partial or total recovery of lattice oxygen. Therefore, steam and air have been used successively to guarantee the recovery of lattice oxygen and adsorbed oxygen in the CL-SMR process. Galinsky [19] used perovskite $CaMn_{1-x}B_xO_{3-\delta}$ as oxygen carriers for chemical looping with oxygen uncoupling. After the reduction step, air is used to regenerate the oxygen carrier while producing heat for power generation. Neal [20] reported that the perovskite support such as $La_{0.8}Sr_{0.2}FeO_3$ (LSF) can enhances the activity of iron oxide for methane conversion by nearly two orders of magnitude. After the partial oxidation of methane using the lattice oxygen in the MeO_x@LSF, the lattice oxygen depleted from the redox catalyst is subsequently regenerated with air in the catalyst regenerator. According to Zhu who used Ce–Fe oxides as oxygen carrier [21], the lattice oxygen of Ce–Fe oxides can be recovered by steam oxidation to the original states; while the high-activity adsorbed oxygen and parts of metal ions are unable to be recovered. The elimination of adsorbed oxygen has a positive effect in the CL-SMR for the generation of target product of syngas. Their results showed that the decrease of CH_4 conversion and increase of CO and H_2 selectivity were just because of the removal of adsorbed oxygen. And the hydrogen generation capacity in the steam oxidation stage had no obvious decline. But the degree of the recovery of lattice oxygen is not discussed.

In the present work, double perovskite-type metal oxide $LaSrFeCoO_6$(LSFCO) made by micro-emulsion method was used as oxygen carrier for the CL-SMR process. The reactivities of $LaSrFeCoO_6$ were investigated in a fixed-bed reactor and the different oxidation routes of steam-oxidation and steam-air stepwise-oxidation were performed to discuss the lattice oxygen recover process. The fresh and reacted oxides were characterized by means of X-ray diffraction (XRD), scanning electron microscopy (SEM), H_2 temperature-programmed reduction (H_2-TPR) techniques, and X-ray photoelectron spectroscopy (XPS), attempting to correlate the activity, structure and surface properties.

2. Experimental

2.1. Synthesis of the double perovskite-type oxide $LaSrFeCoO_6$

Micro-emulsion method was used to prepare the double perovskite-type oxide LSFCO. The required amounts of $La(NO_3)_3{\cdot}6H_2O$, N_2O_6Sr, $CoN_2O_6{\cdot}6H_2O$ and $Fe(NO_3)_3{\cdot}9H_2O$ were weighed at a desired stoichiometric ratio and dissolved in deionized water. Then the surfactant Tritonx-100, cosurfactant n-butyl alcohol and oil phase cyclohexane were added to make a mixture of solution A. Meanwhile, the same ratio of surfactant Tritonx-100, cosurfactant n-butyl alcohol and oil phase cyclohexane were added into $(NH_4)_2CO_3$–NH_4OH to make a mixture of solution B. After that, the solution B was slowly dripped into solution A to form sediment under a water bath at 50 °C. The sediment was allowed to settle for 2 h and filtered by the suction funnel. Then two times of ethanol and deionized water were used to wash the sediment. After that, the sediment was dried overnight in a convection oven at 110 °C. Finally, the as-prepared precursor was thermally decomposed at 500 °C for 2 h and calcined at 1000 °C for 6 h. The resulting product was grounded to obtain the fresh double perovskite-type oxides of LSFCO.

2.2. Characterization

The surface morphology and characteristics of the samples were performed by scanning electron microscopy with energy dispersive X-ray (SEM/EDX) on a Hitachi S4800 instruments. The crystal phases of the oxides were identified by XRD in a Japan Science D/max-R diffractometer with Cu $K\alpha$ radiation ($\lambda = 0.15406$ nm), operating voltage of 40 kV and current of 40 mA, and the diffraction angle (2θ) was scanned from 10° to 80°. The hydrogen-temperature programmed reduction (H_2-TPR) experiments were conducted in 5.0 vol% H_2 balanced with helium at a flow rate of 60 mL/min from room temperature to 800 °C with a heating rate of 10 °C/min. X-ray photoelectron spectroscopy (XPS) was used to probe the near-

surface composition of the oxides. The equipment was Thermo Fisher Scientific Inc with an Al $K\alpha$ X-ray source at an operating voltage of 20 kV and a current of 10 mA, under the conditions of 20 eV and 100 eV pass energy for the survey spectra and the single element spectra.

2.3. Reactivity tests

CL-SMR reactivity evaluation was carried out in a fixed-bed quartz reactor under atmospheric pressure which was reported in our previous work [22]. Methane oxidation activities of the oxides (2 g in each test) were evaluated in a fixed-bed quartz reactor under atmospheric pressure at 850 °C. The flow rate of the feed gas was set at 50 mL/min in which methane was 40.0 vol% and nitrogen gas use as balance gas. The product gases out of the reactor were collected with gas bags and analyzed by a gas chromatograph (Shimadzu GC-2010plus). When the methane conversion step finished, pure N_2 (50 mL/min) was fed to the reactor for 30 min to avoid mixing of gases arising during the two steps. Then the steam generated by injecting demineralized water in an electric furnace at 400 °C using a micro pump was introduced into the reactor for 20 min with N_2 as carrier gas (50 mL/min). The flow rate of the water was controlled at 0.2 mL/min. After CH_4 reduction and steam oxidation, the reacted sample after CH_4–H_2O cycle was named LSFCO-S. Another sample, dry air (50 mL/min) was introduced into the reactor for 10 min after the steam oxidation step, and the reacted sample after CH_4–H_2O-air cycle was named LSFCO-A.

The CH_4 conversion, CO selectivity and H_2 selectivity were calculated as follows:

$$\text{Methane conversion } (\%) = \frac{\text{Moles of methane consumed}}{\text{Moles of methane introduced}} \times 100\% \quad (1)$$

$$\text{CO selectivity } (\%) = \frac{\text{Moles of CO produced}}{\text{Moles of methane consumed}} \times 100\% \quad (2)$$

$$\text{H}_2\text{ selectivity } (\%) = \frac{\text{Moles of H}_2\text{ produced}}{\text{Moles of methane consumed} \times 2} \times 100\%. \quad (3)$$

For the successive CL-SMR cycles, the methane conversion step and steam oxidation step (air oxidation step) were circularly introduced as above.

3. Results and discussions

3.1. SEM-EDS analysis

The morphological features of fresh and reacted oxygen carriers are characterized by SEM as shown in Fig. 2. Besides, the elemental mappings exhibiting the distribution of C in the reacted oxygen carrier particles are analyzed by the SEM-EDX. It can be observed that the three samples are dispersed with mass of holes, which is beneficial for the delivery of oxygen species. The surface of the fresh LSFCO is smooth with distinct connection boundaries. Different sizes of holes are distributed in the grain boundaries with different particle sizes. While after the CH_4 reduction and steam/air oxidation, the surface morphology of samples LSFCO-S and LSFCO-A have no obvious change. But the particle surfaces become slightly rough due to the accumulative effects during the altering reduction and oxidation leading to the crack and interstice of particles. The carbon depositions in the reacted oxygen carriers are illustrated by the SEM-EDX element mapping. It can be seen that the carbon generated from the methane decomposition are distributed uniformly on the reacted oxygen carriers at the micron level. The carbon deposits cannot be completely eliminated by the carbon gasification with steam or carbon oxidation reactions with air. Compared to the sample LSFCO-A, the carbon deposition in the sample LSFCO-S does not appear to be much different. That means the steam plays the same role for the carbon gasification/oxidation as air.

3.2. XRD analysis

The fresh, reduced, and regenerated double perovskite LSFCO were examined by XRD to identify the crystalline phases as shown in Fig. 3. It can be seen from Fig. 3(a) that the XRD pattern of fresh LSFCO is in good agreement with JCPDS (Joint Committee on Powder Diffraction Standards) card 01-075-0541, confirming the formation of the desired perovskite phase with cubic crystal system. Besides, the characteristic peaks of impurity phases at $2\theta = 36°$ and 63° are also observed, representing a mixed metals solid solutions. Generally, the ideal structure of LSFCO may be regarded as a regular arrangement of corner-sharing FeO_6 and CoO_6 octahedra, alternating along three directions of the crystal, with La and Srcations occupying the voids between the octahedral [23,24]. But antisite defects always exist in reality, causing a certain degree of Fe/Co disorder, and consequently leading to the generation of impurity phase. The existence of antisite disorder is inevitable in the double perovskite structure and plays a vital role in their physical properties [25]. Fig. 3(b) shows the XRD pattern of the reduced sample. It can be seen that after exposure to the reducing atmosphere of CH_4, the main structures of double perovskite are obviously changed. The characteristic peaks of La_2O_3, SrO, Fe_2O_3, FeO, CoO, Co^0 and Fe^0 are observed, which are corresponded to the reduction of Fe^{3+} to Fe^{2+}/Fe^0 and Co^{3+} to Co^{2+}/Co^0. While the La^{3+} and Sr^{2+} maintain their valence states and present as the form of La_2O_3 and SrO. Besides, a mixed oxide La_2SrO_x is also observed, supporting the assumption that A-site cations are non-catalytic. Then after the oxidation reactions with steam or steam plus air, two samples LSFCO-S and LSFCO-A recover the double perovskite structures with good regenerability, as shown in Fig. 3(c) and (d). For the sample LSFCO-S after CH_4–H_2O cycle, the characteristic peaks at $2\theta = 36°$ and 42° are emerged, representing the oxide of CoO. It is well know that, cobalt is an element with unstable valence states compared to Fe. It can be easily oxidized or reduced into different valence states such as Co^0, Co^{2+} or Co^{3+} [26]. Therefore, the Co ion cannot incorporate into the double perovskite structure just by the oxidation with weak oxidizing agent steam, and thus form CoO. When the oxygen carrier is further oxidized by air, the characteristic peaks of CoO disappear, and the structure of double perovskite-type recovers to the original state, as shown in Fig. 3(d). Besides, the intensity of the main characteristic peaks for samples LSFCO-S and LSFCO-A all increase compared to the fresh LSFCO, indicating the optimization of crystallinity.

3.3. XPS analysis

The chemical state of the elements and surface composition of the fresh and reacted LSFCO samples were investigated by XPS measurement as shown in Fig. 4. The intensive lines of La 3*d*, Sr 3*d*, Fe 2*p*, Co 2*p*, O 1 s and C 1 s are observed within the binding energy of 0–1400 eV, and no other elements have been detected.

Since the catalytic activity of double perovskite-type oxide is mainly determined by the B′B″ site metals, the valence states of Fe and Co play important roles in the reactivity of double perovskite AA'$FeCoO_6$ oxides. The chemical states of metals Fe and Co in the investigated samples are detailed by fitting the XPS curves as shown in Fig. 5. It can be seen that the XPS patterns of Fe are a double-peaked spectrum with Fe $2p_{3/2}$ at low binding energy and Fe $2p_{1/2}$ at high binding energy. The binding

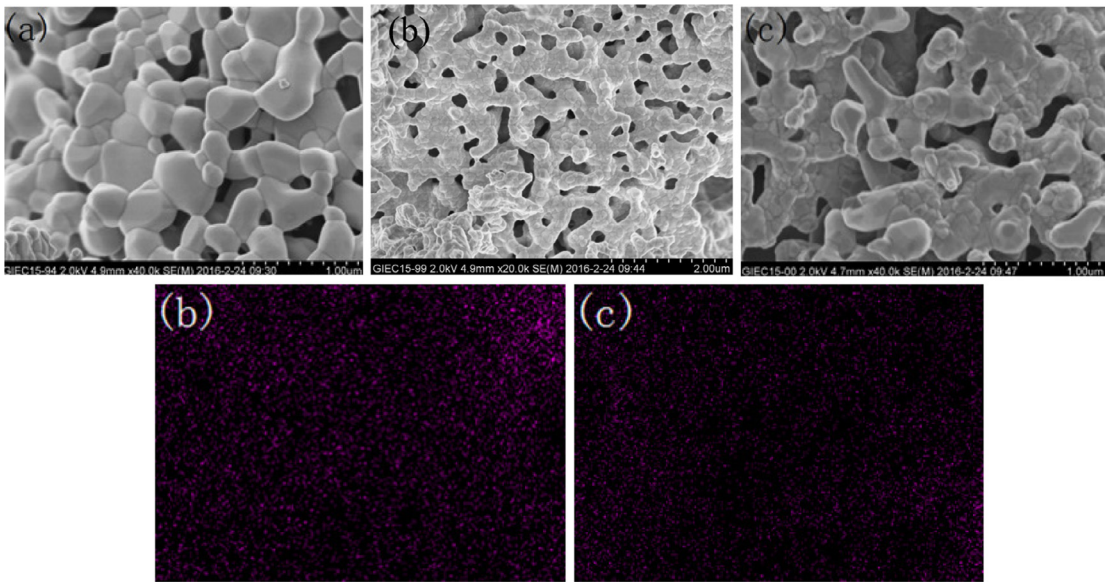

Fig. 2. SEM and carbon mapping of three samples: (a) LSFCO, (b) LSFCO-S, (c) LSFCO-A.

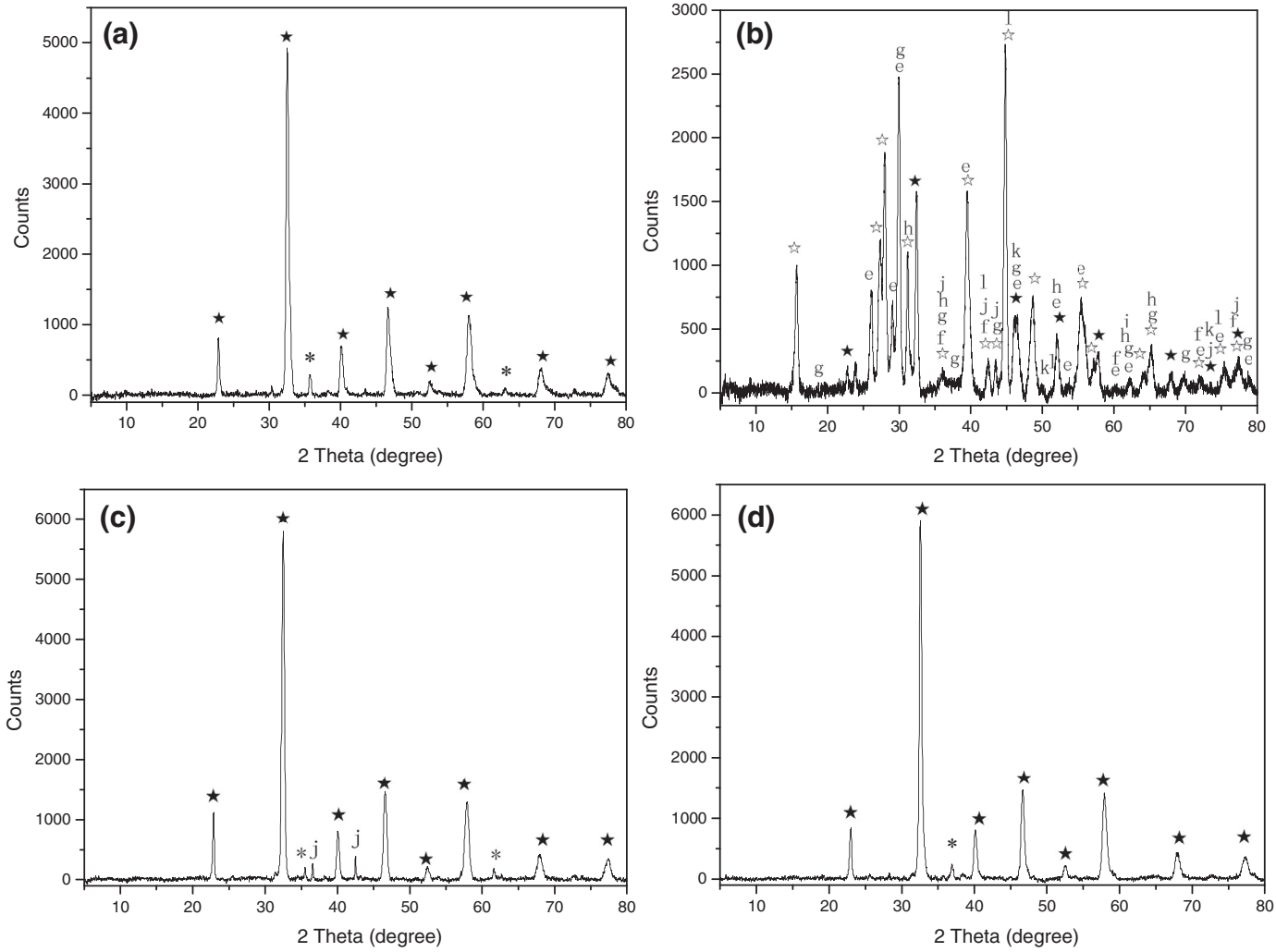

Fig. 3. XRD patterns of samples: (a) LSFCO, (b) Reduced LSFCO, (c) LSFCO-S, (d) LSFCO-A. (⋆) perovskite, (*) impurity phase, (☆) La_2SrO_x, (e) La_2O_3, (f) FeO, (g) Fe_2O_3, (h) SrO, (j) CoO, (k) Fe^0, (l) Co^0.

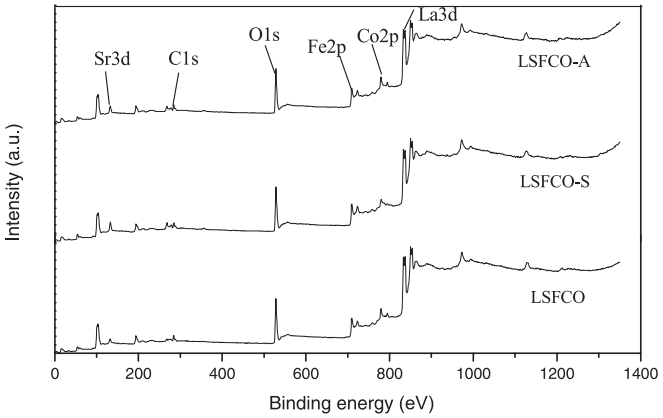

Fig. 4. XPS survey spectrum of three samples.

energy of photoelectron XPS peak of Fe depends mainly on the chemical state of the atoms and molecular environment. The peak positions of Fe $2p_{3/2}$ for samples LSFCO, LSFCO-S and LSFCO-A are 709.48 eV, 709.48 eV and 709.28 eV, respectively. While the peak positions of Fe $2p_{1/2}$ for three samples are 723.08 eV, 723.48 eV and 723.48 eV. They are located between the standard values of Fe^{2+} and Fe^{3+} [27], corresponding to the theory that the asymmetry feature of Fe 2*p* indicating the existence of multiple component of Fe [28]. Moreover, the satellite features presented at the high binding energy sides are also characteristics of Fe^{2+}, Fe^{3+} even Fe^{4+} in an oxide environment. Then the peak fitting method is used to separate the different chemical states of Fe by dividing the integrated areas of peaks. But it is difficult to distinguish the Fe^{4+} from Fe^{3+} and Fe^{2+} just using the XPS technology. Therefore, the peak located at higher binding energy corresponds to Fe^{3+} and Fe^{4+} while the lower energy peak attributes to the Fe^{2+}, because the electron density of Fe^{3+}/ Fe^{4+} is smaller than that of Fe^{2+}. Results show that the $Fe^{2+}/(Fe^{2+}+Fe^{3+}+Fe^{4+})$ ratios of three samples do not appear to be much different from each other, which means that the oxidizing agents steam and air have the same effect on the oxidation of Fe ion in double perovskite-type oxide.

Similarly, the Co 2*p* spectra also exhibit two major peaks with two satellite peaks. The two major components namely Co $2p_{3/2}$ and Co $2p_{1/2}$ are located at 779.20 eV and 794.22 eV for

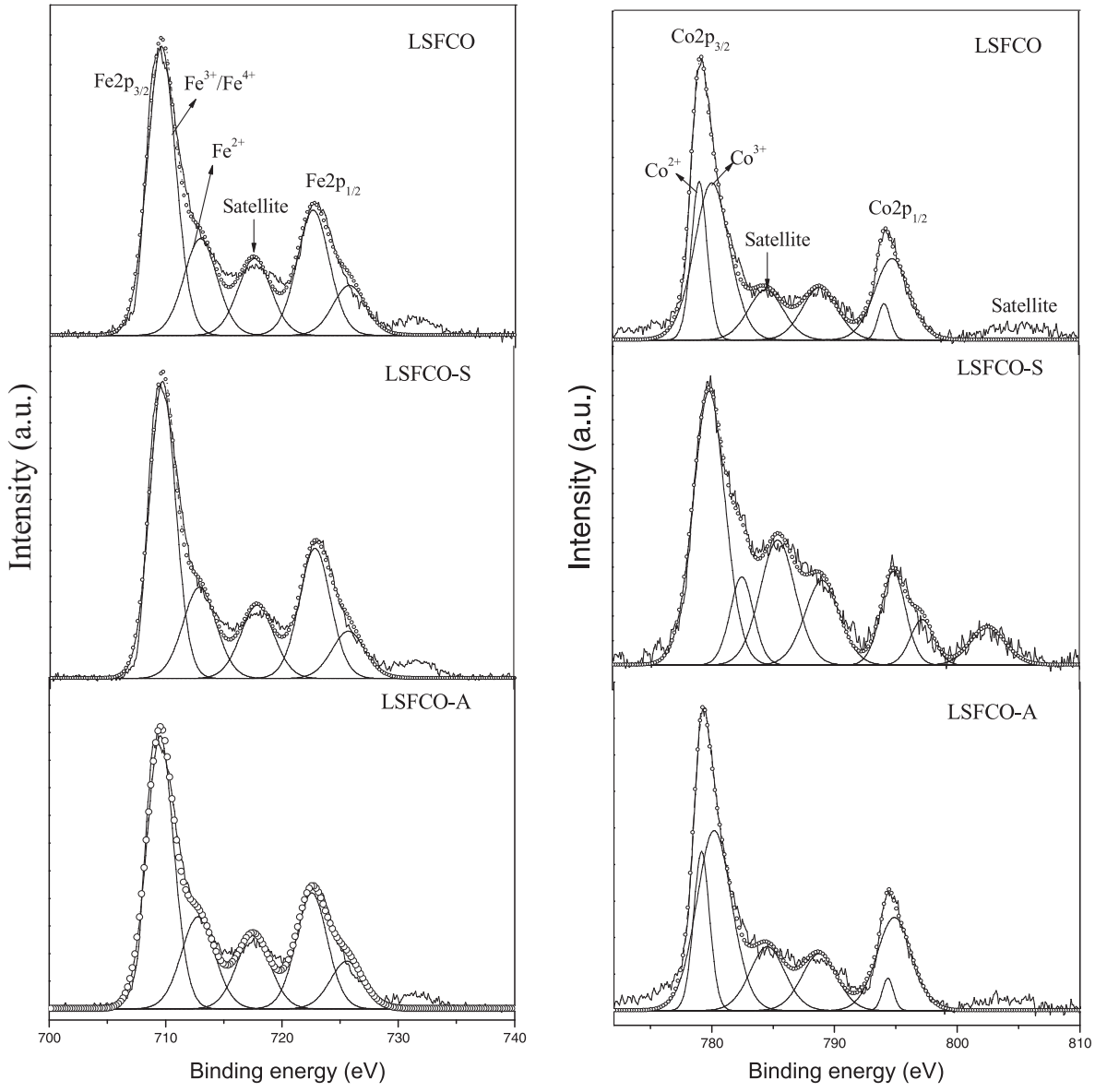

Fig. 5. XPS spectra of Fe 2*p* and Co 2*p* peaks.

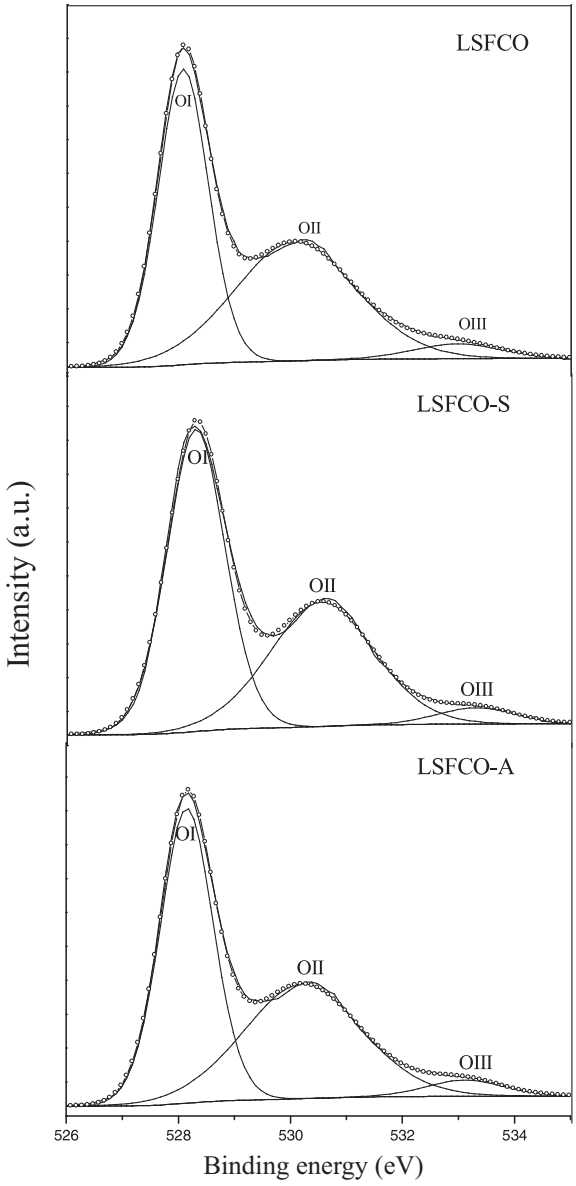

Fig. 6. O 1 s XPS patterns of three samples.

sample LSFCO, 779.92 eV and 794.89 eV for sample LSFCO-S, 779.36 eV and 794.56 eV for sample LSFCO-A, respectively. The values of spin orbit splitting energy of Co $2p_{3/2}$ and Co $2p_{1/2}$ are ~15 eV. The two satellite peaks presented at the high binding energy sides also confirm the existence of mixed oxides with Co^{2+} and Co^{3+}. It should be noted that the XPS peaks of Co $2p_{3/2}$ and Co $2p_{1/2}$ for the sample LSFCO-S is broader than the other two samples, indicating to the existence of additional oxidation state of Co. In the fresh LSFCO, Co^{3+} is the main valence state of Co ion with 23.1% of Co^{2+}. While the Co^{2+}/Co^{3+} ratio increase obviously to 73/27 for the sample LSFCO-S. This result corresponds to the XRD results for the emergence of CoO oxide, whereas Co^{2+} is present. While for the sample LSFCO-A, the Co^{2+}/Co^{3+} ratio goes back to 21/79 and recovers to the original chemical composition almost.

The chemical state O in the investigated samples is given by fitting the XPS curves as shown in Fig. 6, and the relative proportion was calculated on basis of the XPS data (Table 1). The presence of an asymmetry and broadening in the O 1 s spectra is related to the formation of different types of oxygen sites.

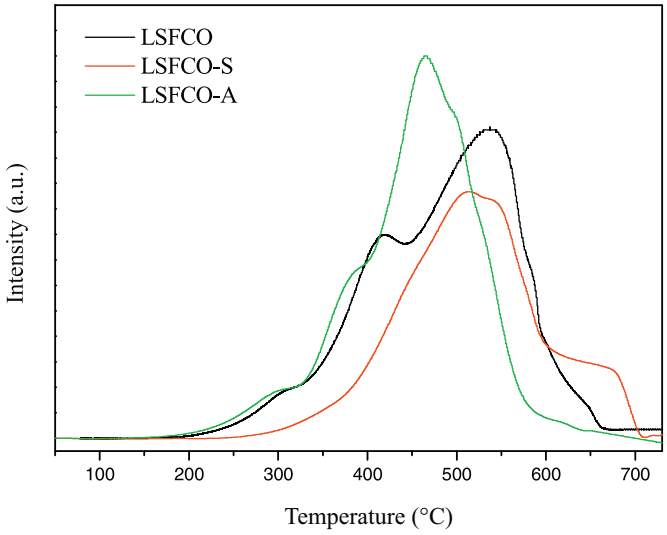

Fig. 7. TPR profiles of three samples.

Three kinds of oxygen species exist in the double perovskite-type oxides, which is lattice oxygen with binding energy < 530.0 eV (denoted as OI), chemisorbed oxygen with binding energy between 530.0–532.0 eV (denoted as OII) and physical adsorbed oxygen with binding energy > 532.0 eV (denoted as OIII), respectively [29]. The lattice oxygen is conducive to the partial oxidation of CH_4 to produce H_2 and CO. The adsorbed oxygen that related to the defect oxides, or surface molecular oxygen with low coordination, is beneficial to the complete oxidation of CH_4 to generate CO_2 and H_2O. According to Tholkappiyan [28], the O 1s spectra that is composed of more than one component peak may be attributed to the oxygen atoms which are bounded to metal ions either covalently (Fe–O–Fe/Co–O–Co/Fe–O–Co) or ionically (Fe=O/Co=O). Different oxygen species could be transformed one to another according to the following pathway: $O_{2(g)} \leftrightarrow O_2^-{}_{(ads)} \leftrightarrow O_2^{2-}{}_{(ads)} \leftrightarrow 2O^-{}_{(ads)} \leftrightarrow 2O^{2-}{}_{(ads)} \leftrightarrow 2O^{2-}{}_{(lat)}$ [29]. The ratio of the integrated areas of the lower and higher binding peaks, OI/(OI+OII+OIII), is 0.69, 0.74 and 0.68 for the samples LSFCO, LSFCO-S and LSFCO-A. The lattice oxygen in the sample LSFCO-S is the highest compared to the other two samples. That means steam is a good oxidizing agent for the recovery of lattice oxygen but a weak oxidant for the adsorbed oxygen recover in the double perovskite-type oxide. The reduced sample oxidized by individual steam exhibits higher lattice oxygen is beneficial for the CH_4 partial oxidation to get the target product of syngas. The total oxygen O 1 s in the LSFCO oxide is 71.25%, compared to 70.1% of total oxygen O 1 s in LSFCO-A, indicating the almost completely recover of the lattice oxygen and adsorbed oxygen after CH_4–H_2O-air cycle.

3.4. H_2-TPR analysis

H_2-TPR was performed aiming to study the reducibility of three samples as shown in Fig. 7. The TPR patterns mainly reflect the reductive property of the B-site metals of Fe and Co, because La and Sr ions in A-site do not take part in the H_2-reduction reaction but just affect the oxygen vacancy and valence states of B-site element. For the fresh LSFCO oxide, two obvious reduction peaks are observed at 419 °C and 540 °C, corresponding to the reduction of $Co^{3+} \rightarrow Co^{2+} \rightarrow Co^0$ and $Fe^{3+} \rightarrow Fe^{2+} \rightarrow Fe^0$. While for the reacted sample LSFCO-A, the boundary of two reduction peaks is not obvious and the peaking temperature shifts to the lower temperature at 466 °C. That means the reduction of Co^{3+} and Fe^{3+} are simultaneously with better reducibility. And it can be more easily reduced compared to the fresh one. This result is corresponded to

Table 1. Data obtained from O 1 s XPS for the samples.

Samples	OI		OII		OIII		OI/(OI+OII+OIII)
	B.E (eV)	Peak area (%)	B.E (eV)	Peak area (%)	B.E (eV)	Peak area (%)	
LSFCO	528.1	48.64	530.3	47.15	533.1	4.21	0.69
LSFCO-S	528.3	55.31	530.1	40.74	533.3	3.95	0.74
LSFCO-A	528.2	51.66	530.2	44.23	533.2	4.11	0.68

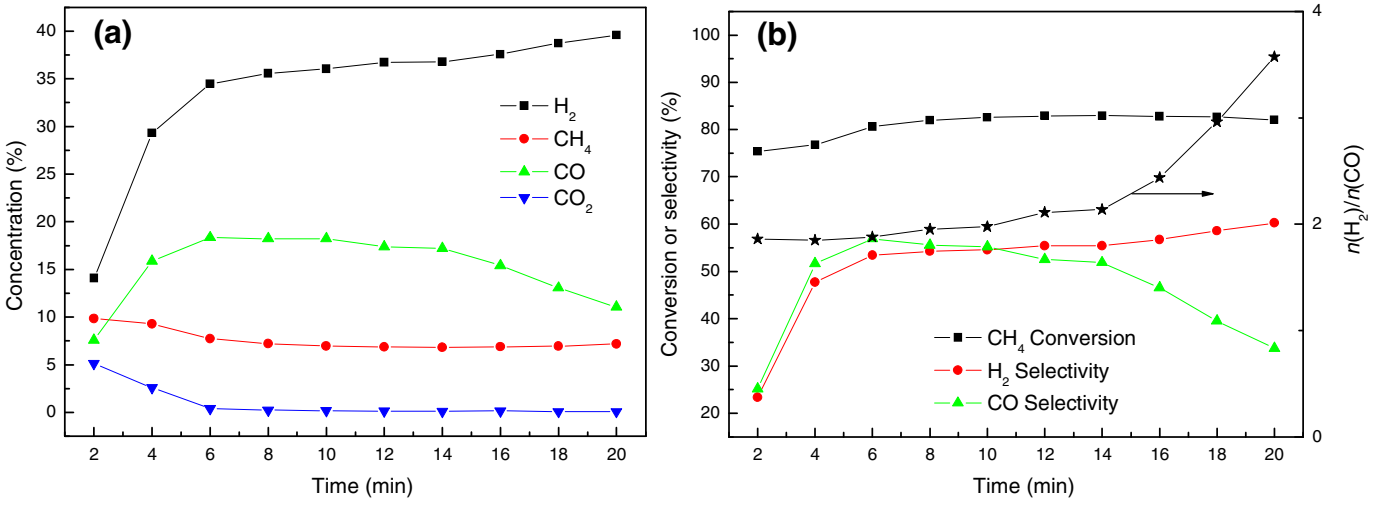

Fig. 8. Catalytic performance as a function of time during methane oxidation reactions.

the XRD message that the reacted sample obtains an optimization of crystallinity after a reduction and oxidation cycle, exhibiting better integration. Some differences are presented for the TPR pattern of sample LSFCO-S, which shows a reduction peak at 514 °C and a peak shoulder after 600 °C. As stated above, the CoO oxide emerges in the sample LSFCO-S and an increase of Co^{2+} is detected by XPS. It is well known that activity of divalent metal ions is lower than that of trivalent metal ions. Therefore the sample LSFCO-S gets more difficult to be reduced due to the emergence of divalent metal Co^{2+}. Moreover, the two reduction peaks are generally associated with the different kinds of oxygen species as mentioned from XPS results. The first reduction peak is primarily attributed to the reduction of non-stoichiometric oxygen and the second reduction peak is associated with the reduction of lattice oxygen. The presence of the second reduction peak and its onset temperature can be adopted as a qualitative description of catalyst reducibility and oxygen mobility within the oxide [30]. Note that the first reduction peak does not appear in the TPR pattern of sample LSFCO-S, indicating the decrease of adsorbed oxygen and the high content of lattice oxygen in it, which is in agreement with the XPS results of O 1 s spectra. The adsorbed oxygen detected by XPS may be generated by the transformation of $O^{2-}_{(ads)} \leftrightarrow O^{2-}_{(lat)}$ and the adsorption of oxygen when exposed to air after reduction.

3.5. Reactivity tests

The redox performances of LSFCO for the production of syngas and hydrogen are shown in Fig. 8. In the reduction stage, the concentrations of H_2 and CO increase rapidly in the earlier stage and go to steady at ~6 min, as shown in Fig. 8(a). Then as the reaction proceeds, the H_2 fraction increases unremittingly but the CO fraction decreases, which are mainly due to the methane decomposition ($CH_4 \rightarrow C+2H_2$). The consumption of CH_4 is relatively stable during the whole reaction at ~75%. Besides, the reaction initially proceeds to high concentrations of CO_2 and decreases sharply to zero after 6th min. That means the adsorbed oxygen which is beneficial for the totally oxidation of CH_4 to CO_2 and H_2O takes a very fast reaction with a higher reactivity. The lattice oxygen that is prone to CH_4 partial oxidation plays a leading role as the adsorbed oxygen depleted. The most important evaluation indexes in the CL-SMR process are the CH_4 conversion and the molar ratio of H_2 to CO. It can be seen from Fig. 8(b), the CH_4 conversion of sample LSFCO reaches at ~80% with the H_2/CO molar ratio at ~2.0 at the initial stage of reaction before 14th min. After 14th min, the H_2/CO molar ratios increase continuously.

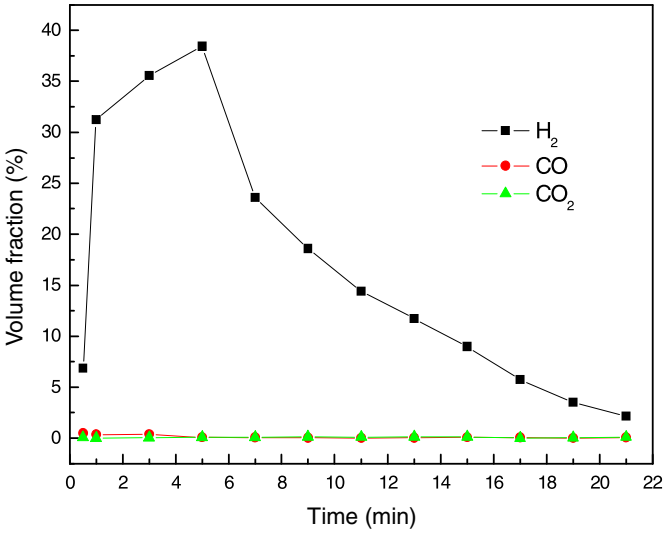

Fig. 9. Gaseous products in steam oxidation step.

In the steam oxidation stage, the oxygen vacancies which are formed due to the remove of [O] in the oxides can be recovered by steam and simultaneously to produce hydrogen. Fig. 9 shows the gaseous products during the steam oxidation step. It can be seen that the hydrogen fraction increases rapidly as the reaction begin and gets the maximum value 38% at ~6 min after

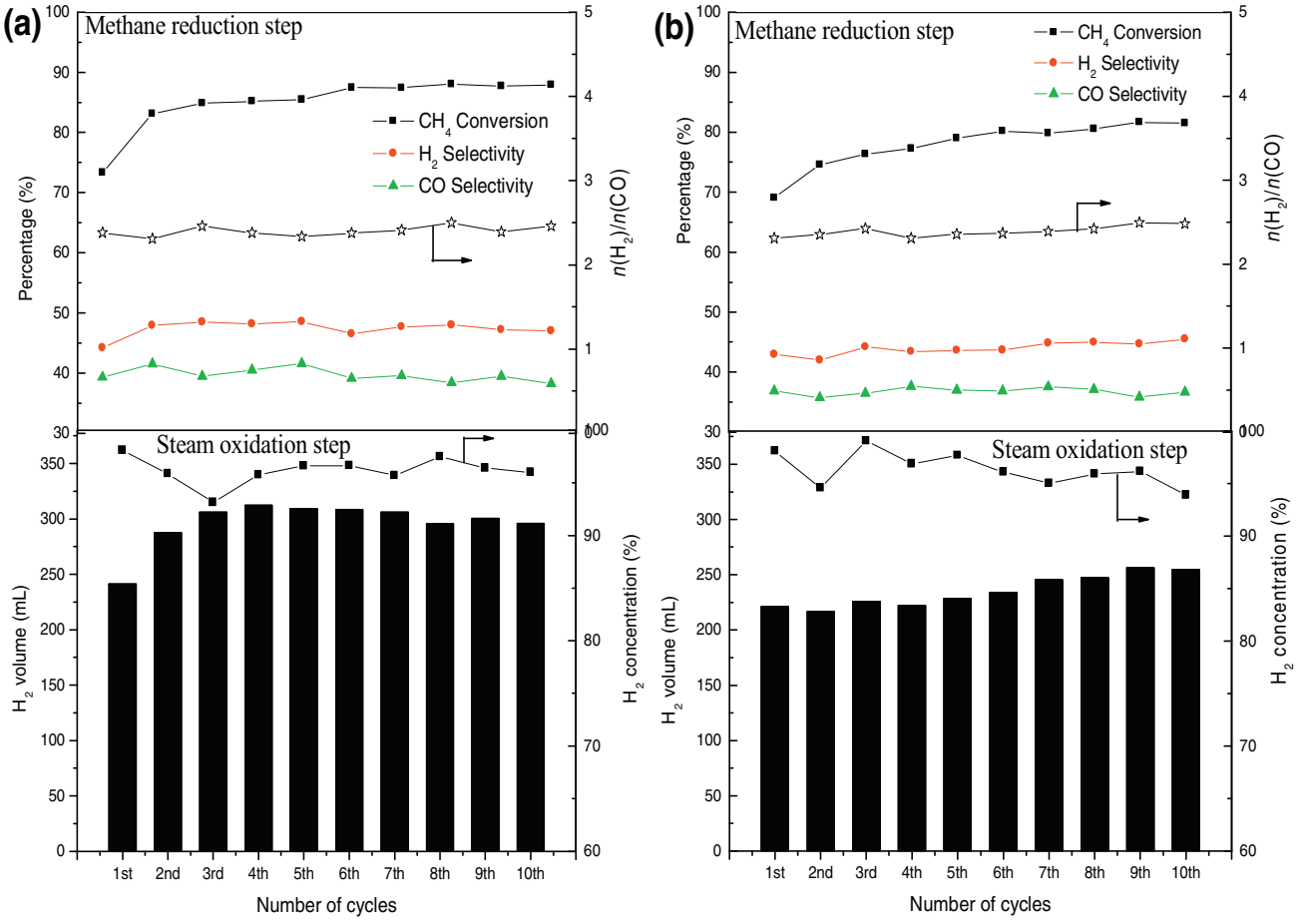

Fig. 10. Comparison of different oxidation routes for LSFCO. (a) CH_4–H_2O cycles, (b) CH_4–H_2O–air cycles.

the reaction start. As the reaction proceeds, the H_2 fractions decrease sharply and close to zero after 20th min. Moreover, a small quantity of CO and CO_2 are observed in the gaseous products, which are aroused by the carbon gasification.

3.6. Successive redox cycle

The alternating methane reducing and steam/air oxidizing reactions were performed on LSFCO to examine its performance for the successive production of syngas and hydrogen. Two different oxidation routes are exploited to discuss the oxygen recovery process during the oxidation step. For the CH_4–H_2O cycles, the reaction time for the methane conversion is controlled for 14 min to avoid excessive carbon deposition, and the water splitting step was fixed at 20 min. Then for the CH_4–H_2O-air cycles, additional 10 min air was introduced. The catalytic performances of two different oxidation routes are shown in Fig. 10. It can be seen that the reactivities of LSFCO in two kinds of cycles kept relatively stable during ten cycles, with good regenerability. For the CH_4–H_2O cycles, syngas with H_2/CO molar ratio close to 2/1 is obtained in the ten cycles with 85% of CH_4 conversion, 94% of CO selectivity, and 47% of H_2 selectivity during the methane reduction step. Then in the steam oxidation step, the average hydrogen volume for 20 min of steam splitting is ~296 mL, with a high hydrogen concentration at ~96%. By contrast for the CH_4–H_2O–air cycle, syngas with H_2/CO molar ratio close to 2/1 is also obtained in the ten cycles. But the CH_4 conversion slightly decreases to 78%, CO selectivity and H_2 selectivity decrease to 44% and 87%, respectively. According to the analysis above, the Co ion cannot incorporate into the double perovskite structure via the individual steam oxidation, which is demonstrated by XRD and XPS tests. The formation of CoO oxide exhibits an obvious effect on the composition of oxygen species in the double perovskite-type oxide. The reduced sample just oxidized by steam has higher lattice oxygen which is advantageous to the CH_4 partial oxidation. Besides, the oxygen content in CoO is 21.35%, which is higher than that in LSFCO, causing the CH_4 conversion increase. Moreover, the hydrogen generation capacity is ~235 mL, also is lower than that in the CH_4–H_2O cycles. As a more active metal, CoO loading on LSFCO also shows a strong reactivity for steam splitting to generate hydrogen. These results indicate that the steam oxidation can effectively recover the structure and reactivity of double perovskite-type oxide. The reduction of adsorbed oxygen in it is beneficial to the partial oxidation of methane to generate syngas. Furthermore, small quantities of CO_2 are also detected during the CH_4–H_2O cycles, with ~15% of CO_2 selectivity. The exists of CO_2 here may not be totally attribute to the oxidation of CH_4 by adsorbed oxygen, but also because of the oxidation by lattice oxygen $[O]_{Fe^*}/[O]_{Co^*}$ with $[CO]_{ads}$: $[O]_{Fe^*}/[O]_{Co^*}+[CO]_{ads}\rightarrow CO_{2(g)}$.

4. Conclusions

The fresh sample LSFCO exhibits a monocrystalline perovskite structure with cubic symmetry and high crystallinity, except for a little impurity phase due to the antisite defect of Fe/Co disorder. After exposure to CH_4 atmosphere, characteristic peaks of Fe_2O_3, FeO, CoO, Co^0 and Fe^0 are presented, indicating the reduction of Fe^{3+} to Fe^{2+}/Fe^0 and the reduction of Co^{3+} to Co^{2+}/Co^0. After the oxidation with steam, the Co ion cannot incorporate into the double perovskite structure and thus form CoO oxide. When the

sample oxidized by steam was further oxidized by air, the characteristic peaks of CoO disappeared, and the structure of double perovskite-type and chemical composition recovered to the original state. By comparison of the two different oxidation routes for the reduced samples, the sample after CH_4–H_2O cycles without air oxidation exhibits higher CH_4 conversion, CO and H_2 selectivity and stronger hydrogen generation capacity, attributed to the formation of the more active oxide CoO, the higher lattice oxygen on LSFCO-S and the minor agglomeration caused by steam oxidation.

Acknowledgments

The financial support of the National Natural Science Foundation of China (51406208, 51406214) is gratefully acknowledged. This work was also supported by the Science & Technology Research Project of Guangdong Province (2015A010106009). We also thank the support of Key Laboratory of Renewable Energy, Chinese Academy of Sciences (Y607j51001).

References

[1] V. Pandey, V. Verma, R.P. Aloysius, G.L. Bhalla, V.P.S. Awana, H. Kishan, R.K. Kotnala, J. Magn. Magn. Mater. 321 (14) (2009) 2239–2244.
[2] M.M. Saad, J. Alloy. Compd. 587 (2014) 652–658.
[3] H. Falcón, J.A. Barbero, G. Araujo, M.T. Casais, M.J. Martıńez-Lope, J.A. Alonso, J.L.G. Fierro, Appl. Catal. B: Environ. 53 (1) (2004) 37–45.
[4] C. Li, W.D. Wang, C.Y. Xu, Y.X. Liu, B. He, C.S. Chen, J. Nat. Gas. Chem. 20 (4) (2011) 345–349.
[5] R.S. Hu, R.R Ding, J. Chen, J.N. Hu, Y.L Zhang, Catal. Commun. 21 (2012) 38–41.
[6] B. Ge, D.S. Ai, J.T. Ma, C.S. Deng, X.P. Lin, J. Rare Earths 29 (7) (2011) 673–677.
[7] R. Egoavil, S. Hühn, M. Jungbauer, N. Gauquelin, A. Béché, G. VanTendeloo, J. Verbeeck, V. Moshnyaga, Nanoscale 7 (21) (2015) 9835–9843.
[8] B. Wiswanathan, Catal. Rev. Sci. Eng. 34 (4) (1992) 337–354.
[9] X. Zhu, Y.G. Wei, H. Wang, K.Z. Li, Int. J. Hydrogen Energy 38 (11) (2013) 4492–4501.
[10] D.H. Lee, K.S. Cha, H.S. Kim, C.S. Park, Y.H. Kim, Int. J. Energy Res. 38 (12) (2014) 1522–1530.
[11] X. Zhu, K.Z. Li, Y.G. Wei, H. Wang, L.Y. Sun, Energy Fuels 28 (2) (2014) 754–760.
[12] K.S. Go, S.R. Son, S.D. Kim, K.S. Kang, C.S. Park, Int. J. Hydrogen Energy 34 (3) (2009) 1301–1309.
[13] S. Bhavsar, G. Veser, RSC Adv. 4 (88) (2014) 47254–47264.
[14] T. Suzuki, O. Nakayama, N. Okamoto, Catal. Surv. Asia 16 (2) (2012) 75–90.
[15] K.S. Cha, B.K. Yoo, H.S. Kim, T.G. Ryu, K.S. Kang, K.S. Park, Y.H. Kim, Int. J. Energy Res. 34 (5) (2010) 422–430.
[16] M.R. Goldwasser, M.E. Rivas, M.L. Lugo, E. Pietri, J. Pérez-Zurita, M.L. Cubeiro, A. Griboval-Constant, G. Leclercq, Catal. Today 107-108 (2005) 106–113.
[17] K. Zhao, F. He, Z. Huang, H.B. Li, Z.L. Zhao, J. Eng. Thermophysics 35 (12) (2014) 2546–2550.
[18] A.R. Kim, H.Y. Lee, D.H. Lee, B.W. Kim, C.H. Chung, D.J. Moon, E.J. Jang, C. Pang, J.W. Bae, Energy Fuels 29 (2) (2015) 1055–1065.
[19] N. Galinsky, M. Sendi, L. Bowers, F.X. Li, Appl. Energy 174 (2016) 80–87.
[20] L. Neal, A. Shafiefarhood, F.X. Li, Appl. Energy 157 (2015) 391–398.
[21] X. Zhu, L.Y. Sun, Y. Zheng, H. Wang, Y.G. Wei, K.Z. Li, Int. J. Hydrogen Energy 39 (25) (2014) 13381–13388.
[22] K. Zhao, F. He, Z. Huang, A.Q. Zheng, H.B. Li, Z.L. Zhao, Int. J. Hydrogen Energy 39 (7) (2014) 3243–3252.
[23] Y.C. Hu, Y.W. Cui, X.W. Wang, Y.P. Liu, Chin. Phys. Lett. 33 (2) (2016) 026101–1–4.
[24] C. Li, W.D. Wang, N. Zhao, Y.X. Liu, B. He, F.C. Hu, C.S. Chen, Appl. Catal. B: Environ. 102 (1/2) (2011) 78–84.
[25] J.K. Murthy, K.D. Chandrasekhar, H.C. Wu, H.D. Yang, J.Y. Lin, A. Venimadhav, J. Phys. Condens. Matter (2016), doi:10.1088/0953-8984/28/8/086003.
[26] W. Haron, T. Thaweechai, W. Wattanathana, A. Laobuthee, H. Manaspiya, C. Veranitisagul, N. Koonsaeng, Energy Procedia. 34 (2013) 791–800.
[27] Peter C.J. Graat, Marcel A.J. Somers, Appl. Surf. Sci. 100/101 (1996) 36–40.
[28] R. Tholkappiyan, K. Vishista, Appl. Surf. Sci. 351 (2015) 1016–1024.
[29] Y.G. Wei, H. Wang, K.Z. Li., J. Rare Earths 28 (4) (2010) 560–565.
[30] F. He, X.A. Li, K. Zhao, Z. Huang, G.Q. Wei, H.B. Li, Fuel 108 (2013) 465–473.